

# Kriging-Based Design for Robust High-Performance Control Systems

Laura Micheli<sup>1</sup> and Simon Laflamme<sup>2</sup>

<sup>1</sup>Assistant Professor, Department of Civil and Environmental Engineering, Catholic University of America, Washington, D.C., 20064, corresponding author; email: michelil@cua.edu

<sup>2</sup>Associate Professor, Department of Civil, Construction, and Environmental Engineering, and Department of Electrical and Computer Engineering, Iowa State University, Ames, IA, 50011; email: laflamme@iastate.edu

## ABSTRACT

High-performance control systems (HPCSs) are sophisticated vibration mitigation devices that include active, semi-active and hybrid systems. HPCSs leverage feedback mechanisms to dynamically adjust the damping force in response to motion, offering a good mitigation performance over a wide excitation bandwidth. These damping systems are attractive for multi-hazard mitigation of civil structures. However, the application of HPCSs necessitates the design and integration of a closed-loop control system that can be susceptible to local failure or reduction in performance in the form of, for example, malfunctions of HPCS components, noisy measurements, wear, aging, and power unavailability. It follows that these sources of uncertainties may cause concerns and impede the wide acceptability and deployment of HPCSs. A solution is to enhance the robustness of the closed-loop configuration through, for example, added redundancies and/or more robust, yet more expensive, components. In this paper, a Kriging-based design procedure is presented enabling the robust design of closed-loop control systems. The design procedure consists of constructing a Kriging surrogate that maps uncertainties to structural performance, and using that surrogate to identify the most influential sources of uncertainties. After, these identified uncertainties are made more robust in order to decrease the variance in the HPCS performance over

the lifetime of the structure. The performance of HPCSs is directly quantified through a life-cycle cost analysis to obtain probability distributions on the expected financial impacts. The proposed procedure is demonstrated on a numerically simulated 39-story structure exposed to wind loads. Uncertainties in both the HPCS configuration (i.e., damping devices and sensors) and external load are considered. Results demonstrate that the proposed framework can be used to substantially improve the robustness of the closed-loop system. Also, through a comparison against a robust passive-viscous case, it is shown that robustly designed HPCSs significantly outperform a passive system in terms of vibration mitigation and life-cycle costs.

**Keywords:** Kriging surrogate, structural control, high performance control system, uncertainty, robust design, semi-active control, vibration mitigation, life-cycle cost analysis

## INTRODUCTION

Structural resilience against natural and man-made hazards can be achieved through the integration of supplemental damping systems. High-performance control systems (HPCSs) are sophisticated motion control devices that can provide supplemental damping through feedback mechanisms and control adaptability. HPCSs, including active, semi-active and hybrid systems, present enhanced mitigation capabilities with respect to passive damping strategies (Dyke and Spencer 1997; Ubertini and Materazzi 2013; Wu and Phillips 2017; Ubertini et al. 2017; Soto and Adeli 2017), and therefore have recently gained popularity for multi-hazards applications for improving structural performance against wind, seismic, and blast loads (He et al. 2003; Lu et al. 2008; Venanzi et al. 2012; Cao et al. 2016) along with reducing life-cycle costs (Wen and Shinozuka 1998; Liu et al. 2004; Goda et al. 2010; Hahm et al. 2015; El-Khoury et al. 2018). While highly promising, these devices are yet to be widely implemented in the field (Casciati et al. 2012), mostly because of the reliance on a feedback loop that creates additional uncertainties (e.g., availability of power, wear, sensor noise, etc.) that are not well understood (Micheli et al. 2020a). It is critical to develop motion-based design methodologies capable of quantifying and optimizing closed-loop control performance under uncertainties in order to fully empower the integration of HPCSs within structural systems.

The problem of uncertainty in structural control is often addressed in literature through proposing robust control strategies (see (Hou and Jin 2011; Drózdź and Szabat 2016; Cao and Laflamme) for instance). More limited work has directly investigated the impact of failure in the closed loop configuration on structural performance. For example Battaini et al. (Battaini et al. 2000) introduced a fault tree approach for actively controlled structures. This approach employed fault patterns, failure rates, and average repair time to assess the reliability of an active control system. Kim et al. (Kim et al. 2013) evaluated the impact of sensor failure on a three-story frame equipped with a magnetorheological damper. The authors utilized fragility functions to demonstrate that the seismic risk of the controlled structure was reduced in comparison with the uncontrolled system, despite faults in the sensor units. Cha and Agrawal (Cha and Agrawal 2014) studied the performance of three different control algorithms subjected to various sensor faults and noise levels on a three-story building equipped with magnetorheological dampers. Their study concluded that the performance degradation was a function of the sensor fault type and control algorithm. The vast majority of the surveyed literature has been devoted to study the effects of sensor failure on HPCS performance. The impact of other uncertainties (e.g., availability of power, wear, aging, etc.) has been overlooked. This could be attributed to the large number of possible scenarios to analyze and relative numerical simulations to perform, which grows exponentially with number of controlled components, controlled floors, and considered hazard events.

In previous works, the authors studied methods to address the computational challenge associated with the integration of closed-loop uncertainties in the analysis of HPCSs. In Ref. (Micheli et al. 2020a), a comparison between deterministic and stochastic methods for reliability analysis was conducted on a 5-story building equipped with semi-active damping devices and subjected to different seismic hazards. Results showed that a proposed modified Monte Carlo simulation strategy, termed bounded Monte Carlo, yielded accurate estimation of the total life-cycle cost of the structure using a relatively small number of simulations. In Ref. (Micheli et al. 2020b), the use of data-driven surrogates (i.e., metamodels) was studied for analyzing uncertainties and identifying the most impactful uncertain variables in the design of an HPCS. Both an offline batch process

and an online sequential process, respectively a Kriging surrogate and an adaptive wavelet network (AWN) surrogate, were developed to map uncertainties in the closed loop configuration and the external load to the maximum structural response. The surrogates were applied to a 39-story building equipped with semi-active damping devices and exposed to wind hazards. The investigation demonstrated that, while the AWN was viable to alleviate the computational demand, Kriging exhibited more accurate mapping and was deemed a more promising tool to identify the most impactful uncertain variables in the closed loop.

This paper builds on previous work to develop a Kriging metamodel-based procedure for robust design of HPCSs, which includes financial and technical analyses based on component redundancy and reliability. The procedure consists of mapping the uncertainties in both the closed-loop configuration and external loads to structural performance using the metamodel, after which the mapping function is used to financially and technically quantify the effect of uncertainties on the system response. The design of the HPCS closed-loop configuration is then altered to enhance its resilience. The proposed design procedure is numerically demonstrated on a 39-story office tower ([Mcnamara and Taylor 2003](#)) located in Boston (MA), used in previous work ([Micheli et al. 2020b](#)). The structure is exposed to wind load, and it is virtually equipped with an HPCS for wind-induced vibrations mitigation.

The rest of the paper is organized as follows. Section 2 introduces the proposed robust design approach and the Kriging model. Section 3 describes the numerical simulation procedure, including the building, excitation, control strategies, and modeled uncertainties. Section 4 presents and discusses the numerical simulation results. Section 5 concludes the paper.

## **ROBUST DESIGN OF HPCS**

In this section, robust design of HPCS under uncertainty is first discussed. After, the metamodeling process is briefly described and the proposed robust design procedure for HPCS is presented.

### **Robust Design of HPCS under Uncertainties**

In general, robust design consists of minimizing the performance variance of a given system and ensuring that the average prescribed performance is met ([Ross 1988](#)). For a structure equipped

with an HPCS, the sources of the performance variance arise from uncertainties in the system, including those from the closed-loop configuration, dynamic parameters, and external excitations. Of interest to this paper are uncertainties inherent to the control system. In previous work (Micheli et al. 2020a), the authors discussed several sources of uncertainties in the closed loop configuration. For example, HPCS components may fail, sensors may have high level of noise or fail, wires can break, power may become unavailable, and damping materials may wear out or leak. This study will also consider uncertainties arising from the external excitations, for instance the intensity of the load.

In the robust design of HPCSs, typical prescribed performance targets  $\mathbf{y}$  are associated with maximum acceleration and/or inter-story drift experienced by the building. Each performance target  $y_i$  has a variance  $\sigma_{y_i}$  that can be reduced through increasing the reliability and/or redundancy of closed-loop components, for example by doubling sensors for each measured state or utilizing a more robust version. However, such design methodology results in additional costs, and one must strategically select which components to improve. In what follows, a Kriging surrogate model-based design procedure is presented to identify uncertain variables that provoke high variability in the system performance in order to improve the robustness of an HPCS. Note that other established techniques to perform sensitivity analysis of engineered systems exist in literature (Saltelli 2002), including Bayesian (Capellari et al. 2016), polynomial chaos-expansion (Sudret 2008; Blatman and Sudret 2010), and Monte Carlo (Zio and Pedroni 2012; Ahmed et al. 2019) approaches. In this study, the surrogate model-based procedure presented in (Micheli et al. 2020b) has been selected to build on findings that Kriging was a computationally fast, accurate and promising tool enabling the robust design of HPCS under uncertainty. The promise of Kriging has been demonstrated in other applications including structural control (Kocijan et al. 2003; Cao et al. 2017; Joy et al. 2018) and structural health monitoring (Laflamme et al. 2016; Fengle et al. 2019).

### **Kriging-based Design for Robust HPCS**

A Kriging metamodel is employed to identify the input variables  $\mathbf{x}$  that have the largest impact on the system response variability. This is done by modeling the effects of uncertainties on the

performance targets  $\mathbf{y}$ , or finding  $f$  such that  $\mathbf{y} = f(\mathbf{x})$ . The overall process is illustrated in Fig. 1, where the surrogate model  $f$  is used to conduct the robust design process. Briefly, the metamodeling process consists of reconstructing the unknown relation between input  $\mathbf{x} \in \mathbb{R}^{k \times N}$  and output  $\mathbf{y} \in \mathbb{R}^{l \times N}$  based on available input/output observations, where  $k$  and  $l$  are the number of input and output variables, respectively, and  $N$  is the number of observations available for the metamodeling process. In this work, the uncertainties in the system are taken as the input  $\mathbf{x}$  of the surrogate and the system performance as its output  $\mathbf{y}$ . The Kriging algorithm used to reconstruct  $y = f(\mathbf{x})$  is reported in Appendix I, where the output  $\mathbf{y}$  is taken as a scalar ( $l = 1$ ) by considering a single performance target for the HPCS design.

Algorithm 1 presents the method used to identify the input variables  $\mathbf{x}$  that have the largest impact on the system response variability, ranking them in order of importance. The first step consists of designing the HPCS to attain target performance requirements (step 1), through an motion-based design procedure for instance (Connor and Laflamme 2014). After, the uncertainties that affect the system response are selected as the inputs  $\mathbf{x}$  (step 2) and a set of inputs/outputs is created exploiting a numerical simulation model of the structure equipped with the HPCS (step 3). This data set is divided in two subsets: training (size  $n$ ) and testing (size  $n_t$ ) data. The Kriging surrogate is then trained on the  $n$  input/output training data (step 4), and its accuracy verified by calculating the root mean square error between simulated and estimated outputs for the  $n_t$  testing data (step 5). Then, a large number ( $n_s$ ) of new input samples is created (step 6), and the corresponding outputs are estimated with the trained Kriging model along with their variance  $\sigma_y^2$  (step 7). Subsequently, each input is sequentially taken as fixed (i.e., no variance), therefore removing the corresponding uncertainties, and the outputs are once again estimated with the Kriging model (step 8). The variance of the new set of outputs is calculated and compared with the variance of the system with uncertainties (step 9). The design variables that lead to the largest differences between variances are identified as the most influential variables (step 10). Note that the use of the surrogate model in lieu of the original numerical simulation model yields significant savings in computational efforts, enabling the evaluation of a large number of uncertainties scenarios in a

relatively short time duration.

---

**Algorithm 1:** Robust design procedure for HPCSs using Kriging-based metamodel.

---

- 1 1: Design HPCS to attain target performance requirements;
  - 2 2: Identify uncertain input variables  $\mathbf{x}$ ;
  - 3 3: Create  $N$  samples  $\{\mathbf{x}, y\}$ ;
  - 4 4: Train Kriging metamodel with  $n$  data (Appendix I);
  - 5 5: Verify accuracy of Kriging with  $n_t$  data;
  - 6 6: Create  $n_s$  new inputs  $\mathbf{x}$ ;
  - 7 7: Estimate corresponding outputs and their variance  $\sigma_y^2$ ;
  - 8 8: **for**  $j = 1: k$  and **for all the**  $n_s$  **do**
  - 9     Fix the  $j$ -th variable at its design value;
  - 10    Predict the output  $y$  with the Kriging metamodel;
  - 11    Estimate variance of the output  $\sigma_{y,j}^2$ ;
  - 12 **end**
  - 13 9: Calculate percentage difference between  $\sigma_y^2$  and  $\sigma_{y,j}^2$ ;
  - 14 10: Identify most influential inputs;
- 

A trivial analytical example is used to illustrate the proposed uncertainties quantification procedure. Consider the following arbitrary function with four variables:

$$f(\mathbf{x}) = 0.25(4 - 4x_1^2 - 2x_2 - 2x_3 - 4x_4^2) \quad (1)$$

where  $x_1, x_2, x_3$ , and  $x_4 \in [0, 1]$ . A training set consisting of  $n = 20$  samples was created by randomly selecting 10 values for  $x_1, x_2, x_3$ , and  $x_4$  within their domain  $[0, 1]$ . The corresponding outputs were calculated using Eq. 1, and the Kriging metamodel trained. The procedure described in steps 6 - 10 of Algorithm 1 was applied, assuming the design value of the  $j$ -th variable as 1. The results of the procedure are reported in Fig. 2, where  $\Delta_v$  indicates the percentage difference between  $\sigma_y^2$  and  $\sigma_{y,j}^2$  obtained from fixing (i.e., no uncertainties)  $\mathbf{x}_j$ . In Fig. 2 (a), one can observe that fixing the variables  $x_1$  and  $x_4$  to their design values yield to the largest change in variance  $\Delta_v$ , and these variables are identified as the most influential, as expected from the analytical formulation. Fig. 2 (b) reports the variance of the system  $\sigma_y^2$  after fixing variables  $x_1$  and  $x_4$ , and variables  $x_2$  and  $x_3$ , showing that the variance is minimized by removing the uncertainties arising from variables  $x_1$  and  $x_4$ .

Once the most influential inputs are identified from Algorithm 1, redundancies in the form of additional elements (e.g., supplemental sensors, utilization of more robust technologies), are integrated in the closed loop configuration. After, a life-cycle cost (LCC) analysis approach (Micheli et al. 2019) is employed to financially quantify the effects of uncertainties and redundancy integration on the system response.

## NUMERICAL CASE STUDY

The proposed analysis and design procedure is demonstrated on a 39-story building equipped with semi-active damping devices for vibration mitigation. The building is subjected to synthetic wind force time series. This section presents the numerical simulation procedure employed in this study, including descriptions of the building model, external excitation, control strategies under investigation, simulated uncertainties, and cost models.

### Building Model

The example building investigated in this study is a 39-story office tower located in Boston (MA) (Mcnamara and Taylor 2003). It is a steel-moment resisting frame, with an octagonal floor plan and a total height of 163 m. The inter-story heights are 7.4 m at the ground and roof levels, and 3.9 m at the other floors. A set of passive damping devices was integrated in the structural system to reduce the structural response of the building to satisfy serviceability criteria under frequent wind hazard events, because wind tunnel tests have shown that the building could have experienced high acceleration levels particularly along its weak axis (McNamara et al. 2000). Therefore, the building was here numerically simulated in its weak direction. A schematic representation of the building equipped with damping devices is reported in Fig. 3. This office tower has been widely studied by the authors because of its known sensitivity to wind excitation. It constitutes a realistic example to benchmark the effectiveness of an HPCS against an existing passive damping system.

The equation of motion is represented in the state-space using a spring-dashpot-mass approximation. For a  $N_f$ -story system equipped with  $N_d$  damping devices, the equations of motion is written (Connor and Laflamme 2014):

$$\mathbf{M}\ddot{\mathbf{u}} + \mathbf{C}\dot{\mathbf{u}} + \mathbf{K}\mathbf{u} = \mathbf{E}_w\mathbf{W} - \mathbf{E}_f\mathbf{F} \quad (2)$$

where  $\mathbf{u} \in \mathbb{R}^{N_f \times 1}$ ,  $\dot{\mathbf{u}} \in \mathbb{R}^{N_f \times 1}$ , and  $\ddot{\mathbf{u}} \in \mathbb{R}^{N_f \times 1}$  are the displacement, velocity and acceleration vectors, respectively, the dot denotes a time derivative,  $\mathbf{W} \in \mathbb{R}^{N_f \times 1}$  is the wind load,  $\mathbf{F} \in \mathbb{R}^{N_d \times 1}$  is the control input vector,  $\mathbf{M} \in \mathbb{R}^{N_f \times N_f}$ ,  $\mathbf{C} \in \mathbb{R}^{N_f \times N_f}$ , and  $\mathbf{K} \in \mathbb{R}^{N_f \times N_f}$  are the mass, damping, and stiffness matrices, respectively,  $\mathbf{E}_w \in \mathbb{R}^{N_f \times N_f}$  and  $\mathbf{E}_f \in \mathbb{R}^{N_f \times N_d}$  are the wind load and the control location matrices, respectively.

The state-space representation of Eq. (2) is given by:

$$\dot{\mathbf{U}} = \mathbf{A}\mathbf{U} + \mathbf{B}_w\mathbf{W} - \mathbf{B}_f\mathbf{F} \quad (3)$$

where  $\mathbf{U} = [\mathbf{u} \quad \dot{\mathbf{u}}]^T \in \mathbb{R}^{2N_f \times 1}$  is the state vector, and with:

$$\mathbf{A} = \begin{bmatrix} \mathbf{0} & \mathbf{I} \\ -\mathbf{M}^{-1}\mathbf{K} & -\mathbf{M}^{-1}\mathbf{C} \end{bmatrix}_{2N_f \times 2N_f} \quad \mathbf{B}_f = \begin{bmatrix} \mathbf{0} \\ \mathbf{M}^{-1}\mathbf{E}_f \end{bmatrix}_{2N_f \times N_d} \quad \mathbf{B}_w = \begin{bmatrix} \mathbf{0} \\ \mathbf{M}^{-1}\mathbf{E}_w \end{bmatrix}_{2N_f \times N_f}$$

The numerical algorithm follows the discrete form of the Duhamel integral ([Connor and Laflamme 2014](#)):

$$\mathbf{U}(t+1) = e^{\mathbf{A}\Delta_t}\mathbf{U}(t) + \mathbf{A}^{-1}(e^{\mathbf{A}\Delta_t} - \mathbf{I})[\mathbf{B}_w\mathbf{W}(t) - \mathbf{B}_f\mathbf{F}(t)] \quad (4)$$

where  $\Delta_t$  is the simulation time interval and  $\mathbf{I} \in \mathbb{R}^{N_f \times N_f}$  is the identity matrix. The inter-story drift is expressed as  $\delta_1 = u_1$  at the first floor and  $\delta_j = u_j - u_{j-1}$  at the other floors. The dynamic properties ( $\mathbf{M}$ ,  $\mathbf{K}$ , and  $\mathbf{C}$ ) of the 39-story buildings can be found in Cao et al. ([Cao et al. 2016](#)). Note that simulations conducted using Eq. 4 assume that the structure remains elastic. This assumption is expected to be valid under wind loads.

## Wind Load

The wind force vector  $\mathbf{W}$  in Eq. 3 is taken as the dynamic component of the along-wind forces acting on the building floors on its weak direction. At the  $j$ -th floor,  $W_j$  is expressed as (Emil and Scanlan 1996):

$$W_j = \rho C_D A_j (V_{m,j} + V_{t,j}) \quad (5)$$

where  $\rho = 1.25 \text{ kg/m}^3$  is the air density,  $C_D = 1.5$  is the drag coefficient,  $A_j$  is the projected area of the building normal to the wind flow,  $V_{m,j}$  is the mean wind speed, and  $V_{t,j}$  is the fluctuating wind velocity generated by the wind turbulence. A logarithmic law is employed to express the mean wind speed at the  $j$ -th floor as (Emil and Scanlan 1996):

$$V_{m,j} = V_{m,10} \frac{\ln(z/z_0)}{\ln(10/z_0)} \quad (6)$$

where  $V_{m,10}$  is the mean wind speed at a reference height  $z = 10 \text{ m}$  above the ground, and  $z_0$  is the terrain roughness ( $=0.03 \text{ m}$ ). Synthetic wind speed time histories are generated as function of  $V_{m,j}$  using the spectral approach outlined in (Deodatis 1996) and reported in (Micheli et al. 2019). Fig. 4 plots two examples of typical wind turbulence  $V_t$  time histories acting on the 36<sup>th</sup> floor of the structure.

## Control Strategies

### *HPCS*

The HPCS of interest to this study is the semi-active damping system proposed by Downey et al. (Downey et al. 2016), termed Banded Rotary Friction Device (BRFD). The BRFD is a variable friction device based on a double wrap band brake system. The dynamic behavior of the BRFD is characterized by a 3-stages dynamic model, summarized as follows (Cao et al. 2015).

Stage 1 is a typical friction dynamics and the damping force  $F_d$  is modeled using a LuGre friction model:

$$\begin{aligned}
F_d &= \sigma_0 \zeta + \sigma_1 \dot{\zeta} + \sigma_2 \dot{\eta} \\
\dot{\zeta} &= \dot{\eta} - \sigma_0 \frac{|\dot{\eta}|}{g(\dot{\eta})} \zeta \\
g(\dot{\eta}) &= F_c + (F_s - F_c) e^{-\left(\frac{\dot{\eta}}{\dot{\eta}_s}\right)^2}
\end{aligned} \tag{7}$$

where  $\sigma_0$  represents the aggregate bristle stiffness,  $\sigma_1$  the microdamping,  $\sigma_2$  the viscous friction,  $\zeta$  an evolutionary variable,  $\dot{\eta}$  the device velocity, and  $g(\dot{\eta})$  is a function that describes the Stribeck effect in which  $\dot{\eta}_s$  is a constant modeling the Stribeck velocity,  $F_s$  the static friction force, and  $F_c$  the kinetic friction force. The value of  $F_c$  is taken as the maximum friction force  $F_{\max}$  (e.g., nominal capacity of the device), and  $F_s = C_s F_{\max}$ , with  $C_s$  being the static friction coefficient.

Stage 2 and 3 are modeled as two linear stiffness regions that represent the backlash effect in the BRFD. The damping force  $F_d$  is modeled as linear stiffness elements  $k_2$  and  $k_3$  during displacements  $d_2$  and  $d_3$  in stages 2 and 3, respectively.

Transition regions are modeled with the following smoothing function

$$\Omega(\eta) = \frac{1}{1 + e^{-\frac{\rho_1(\eta - \eta_0)}{\rho_2}}} \tag{8}$$

where  $\eta_0$  is the reference displacement when transitioning to a new stage, and  $\rho_1$  and  $\rho_2$  are constants. The damping force  $F_d$  within the transition from stage  $i$  to stage  $j$  is written as:

$$F_d = [1 - \Omega(\eta)]F_{d,i} + \Omega(\eta)F_{d,j} \tag{9}$$

Table 1 reports the values of the constants used in the 3-stages dynamic model for the simulated building.

The HPCS configuration virtually installed in the 39-story building consists of 15 sets of two BRFD devices installed at every other floors, starting from the 5<sup>th</sup> floor up to the 33<sup>th</sup> floor (illustrated in Fig. 3), 39 sensors (one per floor), and one global controller. Note that the device locations are the same as those for the viscous damping devices, illustrated in Fig. 3. Furthermore, each set

of devices is numerically simulated as a single device of doubled capacity. The nominal capacity for each set of BRFDs,  $F_{\max}$ , is taken as 1,350 kN for the dampers below the 26<sup>th</sup> floor, and 900 kN for the devices above the 26<sup>th</sup> floor, following the motion-based design provided by the authors in previous studies to satisfy the serviceability-based requirement of a maximum acceleration ( $a_{\text{peak}}$ )  $\leq 25$  mg under frequent wind hazards (Laflamme et al. 2011).

### Controller

A linear quadratic regulator (LQR) algorithm is employed to select the BRFD friction forces, with the intend to use a full-state feedback controller that may be more sensitive to local sensor failure. The LQR has the objective function  $J$ :

$$J = \frac{1}{2} \int (\mathbf{U}^T \mathbf{Q} \mathbf{U} + \mathbf{F}^T \mathbf{R} \mathbf{F}) dt \quad (10)$$

with:

$$\mathbf{Q} = \begin{bmatrix} q_d \mathbf{I} & \mathbf{0} \\ \mathbf{0} & q_v \mathbf{I} \end{bmatrix}_{2N_f \times 2N_f}$$

where  $\mathbf{Q}$  is the regulatory weight matrix with positive definite diagonal elements  $q_d$ ,  $q_v$  and  $\mathbf{R} = q_r \mathbf{I}_{N_f \times N_f}$  is the actuation weight matrix with the positive constant  $q_r$ . The actual control force,  $\mathbf{F}_{d,\text{act}}$ , is written:

$$\begin{aligned} F_{d,\text{act}} &= F_{d,0} v_{\text{act}} \\ \dot{v}_{\text{act}} &= -v_{\text{delay}}(v_{\text{act}} - v_{\text{req}}) \end{aligned} \quad (11)$$

where  $F_{d,\text{act}}$  is the actual control force,  $F_{d,0}$  a voltage scaling constant,  $v_{\text{req}}$  the required voltage computed from the required control force,  $v_{\text{act}}$  the actual voltage in the actuator, and  $v_{\text{delay}}$  a positive constant taken as  $200 \text{ sec}^{-1}$  based on Reference (Cao and Laflamme ).

The required voltage  $v_{\text{req}}$  is computed based on a bang-bang control rule, where the voltage is

set to maximum if the required force  $F_{d,\text{req}}$  is higher than the BRFD capacity and set to zero if the signs of  $F_{d,\text{req}}$  and  $\dot{\delta}_{\text{max}}$  are equal:

$$v_{\text{req}} = \begin{cases} v_{\text{max}} & \text{if } |F_{d,\text{req}}| > F_{d,\text{max}} \\ 0 & \text{if } \text{sign}(\dot{\delta}_{\text{max}}) = \text{sign}(F_{d,\text{req}}) \\ |F_{d,\text{req}}|/F_{d,0} & \text{otherwise} \end{cases} \quad (12)$$

where  $v_{\text{max}}$  is the maximum allowable voltage, taken as 12 V. In the simulations of the 39-story building, the LQR parameters are taken as  $q_d = 4$ ,  $q_v = 1$  and  $q_r = 0.085$  (Micheli et al. 2017).

### *Passive Viscous Dampers*

For the simulations of the passive viscous dampers, a generic viscous damping force is taken as:

$$F_v = c_v \text{sgn}(\dot{u}) \quad (13)$$

where  $c_v$  denotes the damping coefficient,  $\dot{u}$  the relative velocity, and  $\text{sgn}(\dot{u})$  the sign or signum function. The passive viscous dampers configuration follows the BRFDs configuration. Specifically, the damping coefficients are taken as 52,550 kN·s/m for the dampers below the 26<sup>th</sup> floor, and 35,000 kN·s/m for the devices above the 26<sup>th</sup> floor (McNamara et al. 2000; Laflamme et al. 2011). Fig. 5(a) reports a typical force-SDR loops for damping devices under wind load corresponding found at the 23<sup>th</sup> floor corresponding to the location of the largest damping forces. The loops illustrate the similarity in energy dissipation capabilities between the passive and semi-active control strategies.

Fig. 5(b) plots the response profile of the 39-story building exposed to a frequent wind hazard for different control strategies, including that of the BRFD under constant full power (“HPCS passive on”). Results demonstrate that the designed control system is capable of reaching the target performance objective ( $a_{\text{peak}} \leq 25$  mg). One can also notice that the controlled BRFD (“HPCS

LQR”) provides better mitigation capabilities in comparison with ”HPCS passive on” and ”passive viscous” strategies.

### Uncertainty Cases

The three uncertainties cases considered in this study are listed in Table 2. All cases consider uncertainties in the wind load characterized by a variation in the mean wind speed  $V_{m,10}$ , and terrain roughness  $z_0$ , which affect the wind time series generation through Eq. 6 and turbulence simulation process. The mean wind speed is within the range 5-28 m/s, representing the range of wind velocities that the structure will likely experience during its lifespan (Micheli et al. 2019), and the terrain roughness is within the range 0.01-0.03 m, as suggested by (Chuang and Spence 2017).

Cases 1 to 2 are specific to the HPCS, with Case 1 considering uncertainties at the device level, and Case 2 considering uncertainties at the sensor level. Case 1 relates to uncertainties caused by variations in the maximum capacity of the damping devices, which may be caused by different phenomena such as fatigue, excessive load, or degradation of the friction materials. This variation is modeled as a decrease in maximum capacity of a given damping device, with an arbitrarily range between 75% and 100% of  $F_{\max}$ . For uncertainty Case 1, the input vector of the Kriging metamodel is written  $\mathbf{x} = [V_{m,10} \ z_0 \ F_{\max,1} \ F_{\max,2} \ \dots \ F_{\max,15}]^T$ , resulting in  $k = 17$  uncertainty inputs.

Case 2 relates to uncertainties caused by faulty sensors and it is the most computationally expensive. These faults may be caused by wires disconnections and breakage of internal elements from harsh environment, and may yield noisy measurements. Here, these uncertainties are modeled by the addition of uniform random noise in the sensor output  $\mathbf{U}$  (Eq. 3). Different signal-to-noise ratios (SNRs) are simulated, with:

$$\text{SNR} = \left( \frac{A_S}{A_N} \right)^2 \quad (14)$$

where  $A_S$  and  $A_N$  are the root mean squares of the original and noisy sensor signals, respectively. The SNR is bounded between 0.45 (“severe noise”) and 1 (“no noise”) (Cha and Agrawal 2014).

As an example, Fig. 6 reports a typical structural response with under SNR 1.0, 0.70, and 0.45. The input vector under Case 2 is written  $\mathbf{x} = [V_{m,10} \ z_0 \ \text{SNR}_1 \ \text{SNR}_2 \ \dots \ \text{SNR}_{39}]^T$ , yielding  $k = 41$  uncertainty inputs.

Case 3 relates to the passive damping strategy. It only considers the uncertainties related to the wind load, under the assumption that a viscous damper capacity remains invariant during the lifetime of the structure (Taylor Devices 2018), thus yielding  $\mathbf{x} = [V_{m,10} \ z_0]$  or  $k = 2$  uncertainty inputs. Case 3 is used to benchmark the performance of the HPCS.

For each uncertainty case, the Kriging metamodel is trained using  $n$  observations generated by propagating the uncertainties. Specifically, the system is simulated under  $n$  different uncertainty scenarios sampled using the Latin hypercube space filling method from the ranges of variability listed in Table 2, and the corresponding maximum structural response is recorded. The maximum acceleration experienced by the building,  $a_{\text{peak}}$ , is selected as the output to be consistent with the serviceability-based requirement ( $a_{\text{peak}} \leq 25 \text{ mg}$ ). A testing data set composed of  $n_t = 0.25 \ n$  (Friedman et al. 2001) inputs/output observations is created using a similar method to verify the accuracy of the metamodel.

### Life-Cycle Cost Analysis

The LCC of a structure equipped with motion control devices is taken as (Micheli et al. 2019):

$$\text{LCC} = C_0 + C_I + C_M + C_F + C_R \quad (15)$$

where  $C_0$  is the initial cost of the building,  $C_I$  is the initial cost of the motion control system,  $C_M$  is the maintenance cost of the devices,  $C_F$  is the annual failure cost, and  $C_R$  is the redundancies cost. Note that other costs could be integrated in the model depending on the application, such as building retrofit and business relocation costs. The cost  $C_I$  is taken as the sum of the costs of the mechanical devices  $C_D$ , their installation, sensors, and electronics. For a generic viscous damper,  $C_D$  (USD) is computed using (Taflanidis and Gidaris 2013; Taflanidis and Beck 2009):

$$C_D = 0.77F_{\max}^{1.207} + 2806 \quad (16)$$

The cost of the BRFD is estimated as 70% of the cost of a viscous damper with an equivalent  $F_{\max}$ . The 30% discount factor results from the assumption of lower fabrication costs from the relative mechanical simplicity of the BRFD (Micheli et al. 2020a). The cost of a sensor is taken as 2,900 USD, and it includes a lumped cost for the data acquisition systems (Tse et al. 2012). Table 3 lists  $C_I$  values for the HPCS and passive control strategies. These costs do not include supplemental members and connections to install the BRFD devices in the structural frame.

The maintenance cost of the HPCS,  $C_M$ , includes a regular system check and an annual hardware check for 50 years, and is taken as 59,983 USD (adapted from (Tse et al. 2012)). For the viscous strategy, it is assumed that no maintenance is required, with  $C_M = 0$  (Taylor Devices 2018). Cost  $C_F$  quantifies any financial losses occurring from the building not meeting the prescribed performance objective, and it is taken as (Micheli et al. 2019):

$$C_F = \sum_{i=1}^{n_t} C_{\text{fail}}(1+r)^{-i\tau} \quad (17)$$

where  $\tau$  is the cost analysis time interval (taken as  $\tau = 1$  year),  $n_t$  is the lifetime of the structure (taken as  $n_t = 50$  years),  $r$  is the expected rate of return (taken as  $r = 3\%$ ), and  $C_{\text{fail}}$  is defined as (FEMA 2012):

$$C_{\text{fail}} = \sum_{j=1}^{n_h} P_{h,j} \sum_{k=1}^{n_{DS}} P_{DS,k} C_{DS,k} \quad (18)$$

where  $P_{h,j}$  is the annual probability of occurrence of the  $j$ -th hazard event during the lifetime of the structure,  $n_h$  is the number of hazard events considered,  $P_{DS,k}$  and  $C_{DS,k}$  are respectively the probability occurrence and the repair costs associated with the  $k$ -th damage state ( $DS$ ), and  $n_{DS}$  is the total number of damage states considered. The probability  $P_{h,j}$  is obtained using a site-specific hazard curve, while  $DS$  and  $P_{DS,k}$  are estimated combining the structural response of the building, expressed in terms of  $a_{\text{peak}}$ , with fragility curves.

In order to estimate  $P_{DS,k}$ , the peak acceleration  $a_{\text{peak}}$  experienced by the building is estimated using the Kriging surrogate under a selected wind hazard event, and its value is combined with the three fragility curves plotted in Fig. 7(a) to obtain the probability of occurrence of the three damage states  $DS$  ( $n_{DS} = 3$ ). These three fragility curves were developed based on a previous study (Micheli et al. 2019) where the authors thoroughly surveyed existing literature on motion sickness and acceleration thresholds. The figure also reports costs  $C_{DS,k}$ , which are related to the indirect economic losses due to wind-induced motion sickness and discomfort in the building occupants. The cost model employed to calculate  $C_{DS,k}$  as a function of  $a_{\text{peak}}$  is reported in Ref. (Micheli et al. 2019). It assumes that when the building undergoes a certain damage state, the top one third of the building occupants will be subjected to motion sickness, causing losses in working productivity. It also assumes that the mean loss in productivity caused by motion sickness and wind adverse effects (e.g., nausea, fear, sleepiness) is equal to 30% per employee (Lamb and Kwok 2017). Fig. 7(b) plots the hazard curve employed to estimate the probability  $P_h(V_{m,10})$  of the various wind scenarios. This curve was obtained in a previous study by fitting site-specific meteorological data related to the area of Boston with a Weibull distribution (Micheli et al. 2019).

The redundancies cost  $C_R$  depends on the type and number of supplemental components installed in the HPCS. In general,  $C_R$  is estimated summing the costs of redundant components (e.g., sensors, devices). Note that the initial construction cost of the building  $C_0$  is not considered in this investigation, since the purpose of the life-cycle cost analysis is to compare the LCCs of different HPCS configurations, which are not affected by  $C_0$ .

## RESULTS AND DISCUSSION

In this Section, the results of the robust design approach applied to the case study building are presented. First, the accuracy of the Kriging metamodel at reconstructing the unknown input/output relationship is evaluated. Second, the robust design procedure is applied to the HPCS. Third, a life-cycle cost analysis is conducted and the results are presented and discussed.

## Metamodel Validation

The Kriging metamodel is trained on the training data set. After, the testing data set is exploited to verify the generalization capability of the metamodel using two performance metrics: the root mean square error (RMSE), used to quantify the accuracy globally, and the normalized maximum absolute error (NMAE), used to quantify the accuracy locally (Moustapha et al. 2018). The RMSE is defined as:

$$\text{RMSE} = \sqrt{\frac{\sum_{i=1}^{n_t} (y_i - \hat{y}_i)^2}{n_t}} \quad (19)$$

where  $\hat{y}_i$  denotes the maximum structural response estimated by the Kriging model, and  $y_i$  the real or actual maximum structural response obtained from numerical simulations. The NMAE is defined as:

$$\text{NMAE} = \frac{\max |(y_i - \hat{y}_i)|}{n_t \sigma_{n,t}} \quad (20)$$

where  $\sigma_{n,t}$  denotes the standard deviation of the testing data set. A  $k$ -fold (Viana et al. 2009; Forrester and Keane 2009) cross-validation is performed to test the metamodel accuracy over different sections of the training data. The fold size is taken as  $k = 10$ , and the number of samples contained in each fold is set to  $p = 10\%n$ , as recommended in (Viana et al. 2009). The cross-validation error (CRSE) is taken as (Viana et al. 2009):

$$\text{CRSE} = \sqrt{\frac{1}{n} \hat{e}^T \hat{e}} \quad (21)$$

where  $\hat{e} = y_i - \hat{y}_i$ .

Table 4 lists the RMSE, NMAE, and CRSE values, along with the corresponding training and testing data set sizes, for each uncertainty case. Note that the minimum data set size is selected as  $n = 200$  samples and is increased by 200 observations until the RMSE converges to a value  $\leq 10\%$ . This RMSE threshold is set to provide a reasonable trade-off between accuracy and computational

time of the training process. Fig. 8 plots the RMSE and NMAE errors as a function of the training data set size for the HPCS (Cases 1 and 2) and passive viscous strategy (Case 3). Results show that the RMSE and NMAE tend to decrease for increasing number of samples until convergence and oscillation around a given value. This convergence occurs at  $n = 800$  for Cases 1 and 2, and  $n = 400$  for Case 3, which values are taken for subsequent simulations.

Results in Table 4 show that RMSE and NMAE are slightly higher in Case 1 than Case 2. A cross comparison between the HPCS (Cases 1 and 2) and the viscous damping strategy (Case 3) shows that the passive strategy yields a smaller RMSE relative to the HPCS (7.35% and 6.00% for Cases 1 and 2, respectively, versus 4.00% for Case 3), a similar NMAE, and requires a significant smaller number of simulation samples (approximately 50% less). This increase in performance can be attributed to the linear behavior of the damping system and low number of uncertain inputs ( $k = 2$  for Case 3 versus  $k = 17$  and  $k = 41$  for Cases 1 and 2, respectively). The CRSE is relatively small in all of the considered cases, showing that the accuracy of the Kriging metamodel is independent on training sample selection.

The validity of the Kriging model is further assessed by evaluating its capability to reconstruct the standard deviation of the building acceleration  $\sigma_a$ , in addition to the peak value, to determine if the randomness of the wind load is well represented in the surrogate. The training and testing data are augmented with the standard deviation of the acceleration time history response at the floor where  $a_{\text{peak}}$  occurred, with  $\mathbf{y}$  now containing  $\sigma_a$ . The training and testing data sets sizes remain constant. Table 4 lists the RMSE results on  $\sigma_a$ . The RMSE under both Cases 1 and 2 are low (around 6%), comparable to the RMSE of the peak response, thus further demonstrating the validity of the Kriging model.

## Robust Design Results

The verified Kriging surrogate is now used to identify the input variables that cause the highest variability, taken as possible locations for supplemental redundancies. A large number ( $n_s = 5,000$ ) of new input samples is created using the Latin hypercube space filling method from the ranges of variability in Table 2, except for  $V_{m,10}$  that is assumed to follow the Weibull distribution shown in

Fig. 7(b). Following Step 8 of Algorithm 1, the HPCS-related inputs are sequentially fixed at their design values (i.e., no uncertainty), and the corresponding outputs and variances are evaluated with Kriging surrogate. The results of this procedure are reported in Figs. 9(a) and (b) under Cases 1 and 2, respectively.

Fig. 9(a) shows the difference in variance  $\Delta_v$  (%) for the HPCS under Case 1 (damping capacity variability). Large values of  $\Delta_v$  are exhibited under damping devices #4, #10, #14, #8, and #7, which are identified as the most relevant input variables. Under Case 2 (Fig. 9(b)), results identify sensors number #21, #4, # 11, #20, and #34 as being the largest sources of variance. Based on the results presented in Fig. 9(a), 5 out of 15 devices are selected for the redundancies integration. Similarly under Case 2, 5 out of 39 sensors are selected for redundancies integration. Remark that by redundancy integration, it is assumed that secondary devices (Case 1) and sensors (Case 2) are installed at the identified floor locations. Note that strategies other than duplicating a device could be more efficient, such as installing more robust devices or more reliable sensors.

The average structural response and variance of the system with and without redundancies are reported in Table 5, along with the reduction in variance given by the redundancies integration. For verification purposes, results are compared against those obtained using redundancies at locations determined as not influential on the overall variance. These locations are selected as devices #1, #3, #5, #11, and #15 for Case 1, and sensors #6, #8, #28, #31, and #36 for Case 2. The results demonstrate that redundancy yields a significant reduction in variance for both cases. Results also show that the selection of locations not identified as influential does not result in important variance reductions. In all cases, the average response  $\mu_y$  remains approximately the same, as expected.

### Cost Performance

In this section, the cost of an HPCS is estimated considering both the initial configuration ( $C_I$ ) and the configuration with redundancies ( $C_I + C_R$ ). Results, listed in Table 6, indicate that the addition of redundancies in an HPCS configuration yields an increase in  $C_I$  of 24.7% under Case 1 and 8.72% under Case 2.

Subsequently, the cost of failure  $C_{\text{fail}}$  is estimated for  $n_s = 5,000$  scenarios using Eq. 18. Note

that the scenarios are evaluated with the Kriging models along with the corresponding outputs  $a_{\text{peak}}$  experienced by the building. The outputs are used in combination with the fragility curves described in Sec. 3 to obtain damage states and relative failure costs. A Gaussian distribution is then fitted to the resulting  $n_s = 5,000$   $C_{\text{fail}}$ . The results of the cost assessment are reported in Figs. 10 and 11 and compared with the passive strategy (Case 3).

Figs. 10(a) and 11(a) plot the Gaussian distribution fitted to the  $n_s = 5,000$  values of  $C_{\text{fail}}$  obtained with the fragility analysis under Cases 1 and 2, respectively. Results show the probability density function of  $C_{\text{fail}}$  for the initial configuration without redundancies (“0 redundancy”), and three configurations using: 2, 5, 8, and 15 redundancies at the 2, 5, 8, and 15 most influential locations, respectively. The figures also reports the  $C_{\text{fail}}$  distribution for the passive viscous strategy, taken as the benchmark. Results show that, under both Cases 1 and 2, the variance of  $C_{\text{fail}}$  decreases with increasing number of redundancies, while the average cost  $C_{\text{fail}}$  is similar under all the HPCS cases, as expected. A comparison with the passive strategy shows that the HPCS yields a lower  $C_{\text{fail}}$  in terms of both average and variance of the cost distribution when at least two redundancies are added. This could be attributed to the higher mitigation performance under different wind speeds of the HPCS relative to the viscous dampers. Fig. 12 highlights this increase of performance through the profile plots of the maximum accelerations, showing the improvement in performance using the HPCS configuration under different wind speeds.

Figs. 10(b) and 11(b) reports the Gaussian distribution of the LCC under Cases 1 and 2, respectively. The distributions are obtained applying Eq. 17 and 15 to the  $n_s$  scenarios. The figures show that, under both Cases, the impact of redundancies integration is amplified when the  $C_{\text{fail}}$  are projected on the life span of the structure. One can observe that when no redundancies are added in the system, the average LCC of the HPCS is higher than that of the passive strategy, attributed to the higher initial costs and extra maintenance costs. When redundancies are integrated in the system, both average and variance of the HPCS LCC become smaller than that of the passive strategy, yielding important expected financial gains over the projected 50 years of operations. One can also observe that as the number of redundancies increases, the variance of the system decreases,

yielding a more certain expected financial gain but yet at a slightly higher overall average cost due to the cost of redundancies. A cross-comparison between results from Case 1 (Fig. 10) and Case 2 (Fig. 11) show that redundancy in sensors (Case 2) results in a smaller overall gain and loss in LCC variance cost, respectively.

## CONCLUSIONS

This paper introduced a Kriging-based design procedure to improve the robustness of high-performance control systems (HPCS) subjected to uncertainties in their closed-loop configurations. These uncertainties can arise, for example, from possible malfunctions of HPCS components, noisy measurements, wear, aging, and power unavailability. The design procedure consisted of constructing a Kriging surrogate that mapped uncertainties to structural performance, here taken as the peak acceleration, and using that surrogate to identify the most influential sources of uncertainties. After, these identified uncertainties were made more robust through, for example, adding redundancies or increasing the robustness of individual components, in order to decrease the variance in the HPCS performance over the life time of the structure. The performance of HPCSs was directly quantified through a life-cycle cost (LCC) analysis to obtain probability distributions on the expected financial impacts.

The proposed design procedure was demonstrated on a numerically simulated on a 39-story office tower, located in Boston (MA), equipped with a HPCS for wind-induced acceleration reduction. Three different uncertainties cases were investigated. Case 1 included uncertainties in the maximum capacity of the damping devices and on the external load. Case 2 included uncertainties in the sensor measurements and on the external load. Case 3 included uncertainties on the external load only and was used as a benchmark case to simulate the performance of a robust passive viscous system. Results from the training of the Kriging model showed that 800 data points were required to create the representations under Cases 1 and 2, and that 400 data points were required to create the representation under Case 3 due to its simplicity relative to Cases 1 and 2. After, the trained metamodels were employed to compute the maximum structural response under a large number of new input scenarios and to provide an estimate of the system response

variance. The damping devices (Case 1) and sensors (Case 2) that produced the highest variance in structural response were identified as the most influential inputs. Redundancies were integrated at those identified locations and relative costs calculated leveraging the LCC analysis. Results showed that the proposed robustness based design procedure was able to successfully identify the most influential devices/sensors under both Cases 1 and 2. In addition, it was demonstrated that adding redundancies at the most influential locations yielded a significant reduction in the system's variance and LCC, making the structure more significantly resilient using an HPCS relative to a passive viscous system.

Overall, the proposed Kriging-based robust design procedure provided a flexible tool for the design of robust HPCSs to increase structural resiliency. It can also be used to provide important financial data to support the implementation of HPCSs, as demonstrated in this paper through the numerical example. Future work entails the expansion of the methodology to significantly higher dimensional problems, including the co-design of structural elements and control systems.

## **ACKNOWLEDGMENT**

This material is based upon the work supported by the National Science Foundation under Grant No. 1537626. Their support is gratefully acknowledged. Any opinions, findings and conclusions or recommendations expressed in this material do not necessarily reflect the views of the National Science Foundation.

## **DATA AVAILABILITY STATEMENT**

All data, models, or code generated or used during the study are available from the corresponding author by request.

## APPENDIX I. KRIGING ALGORITHM

The Kriging learning algorithm is reported in what follows, taking the performance target as a scalar ( $y$ ). The observation data set available for the metamodeling process is expressed as  $S = \{(\mathbf{x}^{(i)}, y_i), i = 1, \dots, n\}$ , where  $\mathbf{x} = \{x_1, x_2, \dots, x_k\}^T$  is the input vector containing  $k$  variables,  $y_i$  is the corresponding output and  $n$  is the number of training observations. The Kriging process is based on the assumption that the observed response  $y(\mathbf{x})$  follows a stochastic process  $Y(\mathbf{x})$  (Forrester and Keane 2009):

$$Y(\mathbf{x}) = \mu(\mathbf{x}) + Z(\mathbf{x}) \quad (22)$$

where  $\mu(\mathbf{x})$  is the mean of the process and  $Z(\mathbf{x})$  is its deviation from the mean assumed to follow a Gaussian process with zero mean and covariance matrix  $\mathbf{D}$ :

$$\mathbf{D} = \sigma^2 \Psi \quad (23)$$

where  $\sigma^2$  is the variance of the process, and  $\Psi \in \mathbb{S}^{n \times n}$  is the correlation matrix. For  $n$  observations,  $\Psi$  is given by:

$$\Psi = \begin{pmatrix} \psi[Y(\mathbf{x}^{(1)}), Y(\mathbf{x}^{(1)})] & \dots & \psi[Y(\mathbf{x}^{(1)}), Y(\mathbf{x}^{(n)})] \\ \vdots & \ddots & \vdots \\ \psi[Y(\mathbf{x}^{(n)}), Y(\mathbf{x}^{(1)})] & \dots & \psi[Y(\mathbf{x}^{(n)}), Y(\mathbf{x}^{(n)})] \end{pmatrix} \quad (24)$$

In Eq. 24, the Gaussian correlation function  $\psi$  is written:

$$\psi[Y(\mathbf{x}^{(p)}), Y(\mathbf{x}^{(q)})] = \exp\left(-\sum_{j=1}^k \theta_j |x_j^{(p)} - x_j^{(q)}|^2\right) \quad (25)$$

where  $\psi[Y(\mathbf{x}^{(p)}), Y(\mathbf{x}^{(q)})]$ ,  $p, q = 1, \dots, n$  are observations of the stochastic process,  $k$  is the number of input variables, and  $\theta_j$ ,  $j = 1, \dots, k$  are the hyper-parameters of the correlation function. The hyper-parameters of the Kriging function can be estimated employing the maximum likelihood method (Forrester et al. 2008), where the likelihood function  $L$  can be written as a function

of the observations:

$$L = \frac{1}{(2\pi\sigma^2)^{n/2}|\Psi|^{1/2}} \exp \left[ -\frac{(\mathbf{y} - \mathbf{1}\mu)^T \Psi^{-1} (\mathbf{y} - \mathbf{1}\mu)}{(2\sigma^2)} \right] \quad (26)$$

It can be demonstrated that the maximum likelihood estimates of the mean and standard deviation are (Forrester et al. 2008):

$$\hat{\sigma}^2 = \frac{1}{n} (\mathbf{y} - \mathbf{1}\mu)^T \Psi^{-1} (\mathbf{y} - \mathbf{1}\mu) \quad (27)$$

$$\hat{\mu} = \frac{\mathbf{1}^T \Psi^{-1} \mathbf{y}}{\mathbf{1}^T \Psi^{-1} \mathbf{1}} \quad (28)$$

where the hat denotes an estimate, and  $\mathbf{1} \in \mathbb{R}^{N \times 1}$  is a vector of ones. Note that  $\Psi$ , and therefore  $\hat{\mu}$  and  $\hat{\sigma}^2$ , depends on the unknown hyper-parameters  $\theta_j$ , which can be evaluated using an optimization algorithm to maximize Eq. 26 after substituting Eqs. 27 and 28 into Eq. 26. Here, a genetic optimization algorithm is selected to solve the maximum likelihood optimization problem in Eq. 26 and estimate  $\theta_j$ . Furthermore, in the event where two samples are very close to each other, the nearest symmetric positive matrix is used for matrix  $\Psi$  (Higham 1988) to prevent the correlation matrix in Eq. 24 from becoming poorly conditioned.

## REFERENCES

- Ahmed, Q. A., Nimir, H. B., Ayoub, M. A., and Mohyaldinn, M. E. (2019). "Application of variance-based sensitivity analysis in modeling oil well productivity and injectivity." Journal of Petroleum Exploration and Production Technology, 1–10.
- Battaini, M., Casciati, F., and Faravelli, L. (2000). "Some reliability aspects in structural control." Probabilistic Engineering Mechanics, 15(1), 101–107.
- Blatman, G. and Sudret, B. (2010). "Efficient computation of global sensitivity indices using sparse polynomial chaos expansions." Reliability Engineering & System Safety, 95(11), 1216–1229.
- Cao, G., Lai, E. M.-K., and Alam, F. (2017). "Gaussian process model predictive control of an unmanned quadrotor." Journal of Intelligent & Robotic Systems, 88(1), 147–162.
- Cao, L., Downey, A., Laflamme, S., Taylor, D., and Ricles, J. (2015). "Variable friction device for structural control based on duo-servo vehicle brake: Modeling and experimental validation." Journal of Sound and Vibration, 348, 41–56.
- Cao, L. and Laflamme, S. "Real-time variable multi-delay controller for multi-hazard mitigation." Journal of engineering mechanics.
- Cao, L., Laflamme, S., Taylor, D., and Ricles, J. (2016). "Simulations of a variable friction device for multihazard mitigation." Journal of Structural Engineering, 142(12), H4016001.
- Capellari, G., Chatzi, E., and Mariani, S. (2016). "Optimal sensor placement through bayesian experimental design: Effect of measurement noise and number of sensors." Multidisciplinary Digital Publishing Institute Proceedings, Vol. 1, 41.
- Casciati, F., Rodellar, J., and Yildirim, U. (2012). "Active and semi-active control of structures – theory and applications: A review of recent advances." Journal of Intelligent Material Systems and Structures, 23(11), 1181–1195.
- Cha, Y.-J. and Agrawal, A. K. (2014). "Robustness studies of sensor faults and noises for semi-active control strategies using large-scale magnetorheological dampers." Journal of Vibration and Control, 22(5), 1228–1243.
- Chuang, W.-C. and Spence, S. M. (2017). "A performance-based design framework for the inte-

- grated collapse and non-collapse assessment of wind excited buildings.” Engineering Structures, 150, 746–758.
- Connor, J. and Laflamme, S. (2014). Structural motion engineering. Springer.
- Deodatis, G. (1996). “Simulation of ergodic multivariate stochastic processes.” Journal of engineering mechanics, 122(8), 778–787.
- Downey, A., Cao, L., Laflamme, S., Taylor, D., and Ricles, J. (2016). “High capacity variable friction damper based on band brake technology.” Engineering Structures, 113, 287–298.
- Drózdź, K. and Szabat, K. (2016). “Application of unscented kalman filter in adaptive control structure of two-mass system.” 2016 IEEE International Power Electronics and Motion Control Conference (PEMC), IEEE, 1150–1154.
- Dyke, S. and Spencer, B. (1997). “A comparison of semi-active control strategies for the mr damper.” Proceedings Intelligent Information Systems. IIS’97, IEEE, 580–584.
- El-Khoury, O., Shafieezadeh, A., and Fereshtehnejad, E. (2018). “A risk-based life cycle cost strategy for optimal design and evaluation of control methods for nonlinear structures.” Earthquake Engineering & Structural Dynamics, 47(11), 2297–2314.
- Emil, S. and Scanlan, R. H. (1996). “Wind effects on structures: fundamentals and applications to design.
- FEMA, P. (2012). “58 (2012).” Seismic performance assessment of buildings. Prepared by Applied Technology Council as ATC, 58.
- Fengle, X., Zhansi, J., Jiawei, X., and Shuilong, H. (2019). “An improved two-step method based on kriging model for beam structures.” Journal of Low Frequency Noise, Vibration and Active Control, 38(3-4), 1378–1390.
- Forrester, A., Sobester, A., and Keane, A. (2008). Engineering design via surrogate modelling: a practical guide. John Wiley & Sons.
- Forrester, A. I. and Keane, A. J. (2009). “Recent advances in surrogate-based optimization.” Progress in aerospace sciences, 45(1-3), 50–79.
- Friedman, J., Hastie, T., and Tibshirani, R. (2001). The elements of statistical learning, Vol. 1.

Springer series in statistics New York.

- Goda, K., Lee, C., and Hong, H. (2010). “Lifecycle cost–benefit analysis of isolated buildings.” Structural Safety, 32(1), 52–63.
- Hahm, D., Koh, H., Ok, S., Park, W., Chung, C., and Park, K. (2015). “Cost-effectiveness evaluation of mr damper system for cable-stayed bridges under earthquake excitation.” Advances in Bridge Maintenance, Safety Management, and Life-Cycle Performance, Set of Book & CD-ROM: Proceedings of the Third International Conference on Bridge Maintenance, Safety and Management, 16-19 July 2006, Porto, Portugal-IABMAS’06, CRC Press, 301.
- He, W. L., Agrawal, A. K., and Yang, J. N. (2003). “Novel semiactive friction controller for linear structures against earthquakes.” Journal of Structural Engineering, 129(7), 941–950.
- Higham, N. J. (1988). “Computing a nearest symmetric positive semidefinite matrix.” Linear algebra and its applications, 103, 103–118.
- Hou, Z. and Jin, S. (2011). “Data-driven model-free adaptive control for a class of mimo nonlinear discrete-time systems.” IEEE Transactions on Neural Networks, 22(12), 2173–2188.
- Joy, E. J., Menon, A. S., and Biju, N. (2018). “Implementation of kriging surrogate models for delamination detection in composite structures.” Advanced Composites Letters, 27(6), 096369351802700604.
- Kim, Y., Bai, J.-W., and Albano, L. D. (2013). “Fragility estimates of smart structures with sensor faults.” Smart Materials and Structures, 22(12), 125012.
- Kocijan, J., Murray-Smith, R., Rasmussen, C. E., and Likar, B. (2003). “Predictive control with gaussian process models.” The IEEE Region 8 EUROCON 2003. Computer as a Tool., Vol. 1, IEEE, 352–356.
- Laflamme, S., Cao, L., Chatzi, E., and Ubertini, F. (2016). “Damage detection and localization from dense network of strain sensors.” Shock and Vibration, 2016.
- Laflamme, S., Taylor, D., Maane, M. A., and Connor, J. J. (2011). “Modified friction device for control of large-scale systems.” Structural Control and Health Monitoring, 19(4), 548–564.
- Lamb, S. and Kwok, K. C. (2017). “Sopite syndrome in wind-excited buildings: productivity and

- wellbeing impacts.” Building Research & Information, 45(3), 347–358.
- Liu, M., Wen, Y., and Burns, S. A. (2004). “Life cycle cost oriented seismic design optimization of steel moment frame structures with risk-taking preference.” Engineering Structures, 26(10), 1407–1421.
- Lu, L.-Y., Lin, G.-L., and Kuo, T.-C. (2008). “Stiffness controllable isolation system for near-fault seismic isolation.” Engineering Structures, 30(3), 747–765.
- McNamara, R., Huang, C., and Wan, V. (2000). “Viscous-damper with motion amplification device for high rise building applications.” Advanced Technology in Structural Engineering, 1–10.
- Mcnamara, R. J. and Taylor, D. P. (2003). “Fluid viscous dampers for high-rise buildings.” The structural design of tall and special buildings, 12(2), 145–154.
- Micheli, L., Alipour, A., Laflamme, S., and Sarkar, P. (2019). “Performance-based design with life-cycle cost assessment for damping systems integrated in wind excited tall buildings.” Engineering Structures, 195, 438–451.
- Micheli, L., Cao, L., Gong, Y., Cancelli, A., Laflamme, S., and Alipour, A. (2017). “Probabilistic performance-based design for high performance control systems.” Active and Passive Smart Structures and Integrated Systems 2017, Vol. 10164, SPIE, 101642I (apr).
- Micheli, L., Cao, L., Laflamme, S., and Alipour, A. (2020a). “Life-cycle cost evaluation strategy for high-performance control systems under uncertainties.” Journal of Engineering Mechanics, 146(2), 04019134.
- Micheli, L., Hong, J., Laflamme, S., and Alipour, A. (2020b). “Surrogate models for high performance control systems in wind-excited tall buildings.” Applied Soft Computing, 106133.
- Moustapha, M., Bourinet, J.-M., Guillaume, B., and Sudret, B. (2018). “Comparative study of kriging and support vector regression for structural engineering applications.” ASCE-ASME Journal of Risk and Uncertainty in Engineering Systems, Part A: Civil Engineering, 4(2), 04018005.
- Ross, P. J. (1988). Taguchi techniques for quality engineering: loss function, orthogonal experiments, parameter and tolerance design. Number TS156 R12. McGraw-Hill New York.
- Saltelli, A. (2002). “Sensitivity analysis for importance assessment.” Risk analysis, 22(3), 579–

590.

- Soto, M. G. and Adeli, H. (2017). “Many-objective control optimization of high-rise building structures using replicator dynamics and neural dynamics model.” Structural and Multidisciplinary Optimization, 56(6), 1521–1537.
- Sudret, B. (2008). “Global sensitivity analysis using polynomial chaos expansions.” Reliability engineering & system safety, 93(7), 964–979.
- Taflanidis, A. A. and Beck, J. L. (2009). “Life-cycle cost optimal design of passive dissipative devices.” Structural Safety, 31(6), 508–522.
- Taflanidis, A. A. and Gidaris, I. (2013). “Life-cycle cost based optimal retrofitting of structures by fluid dampers.” Structures Congress 2013, American Society of Civil Engineers (apr).
- Taylor Devices, W. (accessed March 8, 2018). Seismic Dampers and Seismic Protection Products, <<http://taylordevices.com/dampers-seismic-protection.html>>.
- Tse, K. T., Kwok, K. C. S., and Tamura, Y. (2012). “Performance and cost evaluation of a smart tuned mass damper for suppressing wind-induced lateral-torsional motion of tall structures.” Journal of Structural Engineering, 138(4), 514–525.
- Ubertini, F., Comanducci, G., and Laflamme, S. (2017). “A parametric study on reliability-based tuned-mass damper design against bridge flutter.” Journal of Vibration and Control, 23(9), 1518–1534.
- Ubertini, F. and Materazzi, A. L. (2013). “Seismic response control of buildings with force saturation constraints.” Smart Structures and Systems, 12(2), 157–179.
- Venanzi, I., Ubertini, F., and Materazzi, A. L. (2012). “Optimal design of an array of active tuned mass dampers for wind-exposed high-rise buildings.” Structural Control and Health Monitoring, 20(6), 903–917.
- Viana, F. A., Haftka, R. T., and Steffen, V. (2009). “Multiple surrogates: how cross-validation errors can help us to obtain the best predictor.” Structural and Multidisciplinary Optimization, 39(4), 439–457.
- Wen, Y. and Shinozuka, M. (1998). “Cost-effectiveness in active structural control.” Engineering

Structures, 20(3), 216–221.

Wu, J. and Phillips, B. M. (2017). “Passive self-centering hysteretic damping brace based on the elastic buckling mode jump mechanism of a capped column.” Engineering Structures, 134, 276–288.

Zio, E. and Pedroni, N. (2012). “Monte carlo simulation-based sensitivity analysis of the model of a thermal–hydraulic passive system.” Reliability Engineering & System Safety, 107, 90–106.

**List of Tables**

1	BRFD friction model parameters . . . . .	33
2	Uncertainties cases and ranges of variability . . . . .	34
3	Initial installation costs . . . . .	35
4	Performance of the Kriging surrogate. . . . .	36
5	Variance reduction under redundancies. . . . .	37
6	Costs of HPCS with and without redundancies . . . . .	38

TABLE 1: BRFD friction model parameters

Parameter	Value	Unit
$\sigma_0$	7005	$\text{kN}^{-1}$
$\sigma_1$	0.0017	$\text{N}^{-1}$
$\sigma_2$	0.0017	$\text{N}^{-1}$
$\dot{\eta}_s$	0.002	$\text{m}\cdot\text{s}^{-1}$
$C_s$	1.065	—
$k_2$	0.03	$\text{kN}\cdot\text{mm}^{-1}$
$k_3$	2.3	$\text{kN}\cdot\text{mm}^{-1}$
$d_2$	3.05	mm
$d_3$	1.52	mm
$\rho_1$	0.1	mm
$\rho_2$	0.01	mm

TABLE 2: Uncertainties cases and ranges of variability

Case	Variables	Symbol	Range of variability	N. variables
1	Mean wind speed	$V_{m,10}$	5 - 28 m/s	$k = 17$
	Terrain roughness	$z_0$	0.01 - 0.03 m	
	Damper capacity	$F_{\max}$	$[0.75 \ 1] F_{\max}$	
2	Mean wind speed	$V_{m,10}$	5 - 28 m/s	$k = 41$
	Terrain roughness	$z_0$	0.01 - 0.03 m	
	Noise	SNR	0.45 - 1.00	
3	Mean wind speed	$V_{m,10}$	5 - 28 m/s	$k = 2$
	Terrain roughness	$z_0$	0.01 - 0.03 m	

TABLE 3: Initial installation costs

Component	$C_I$ (USD) HPCS	$C_I$ (USD) passive
Mechanical devices ( $C_D$ )	86,898	124,138
Sensors and electronics	113,750	0
Total	200,647	124,138

TABLE 4: Performance of the Kriging surrogate.

Case	Training $n$	Testing $n_t$	RMSE (%)	NMAE (%)	CRSE (mg)	RMSE $_{\sigma_a}$ (%)
1 (HPCS)	800	200	7.35	0.54	2.02	6.09
2 (HPCS)	800	200	6.00	0.40	2.18	5.89
3 (passive)	400	100	4.00	0.50	0.20	3.33

TABLE 5: Variance reduction under redundancies.

Case	Configuration	Mean, $\mu_y$ (mg)	Variance, $\sigma_y^2$ (mg)	Variance reduction (%)
1	Initial configuration	15.00	6.62	-
	Redundancies at #4, #7, #8, #10, and #14	15.87	3.89	41.18
	Redundancies at #1, #3, #5, #11, and #15	15.32	6.67	2.58
2	Initial configuration	14.84	4.81	-
	Redundancies at #4, #11, #20, #21, and #34	14.45	2.71	43.52
	Redundancies at #6, #8, #28, #31 and #36	14.45	4.83	0.43

TABLE 6: Costs of HPCS with and without redundancies

Case	$C_I$ (USD)	$C_R$ (USD)	$C_I + C_R$ (USD)
1	200,647	49,512	250,159
2	200,647	17,500	218,147

## List of Figures

1	Schematic illustration of robust design methodology for HPCS systems under uncertainties. . . . .	41
2	Analysis of function from Eq. 1: (a) identification of most influential variables; and (b) variance of the system fixing different variables. . . . .	42
3	Schematic representation of the case study building. . . . .	43
4	Examples of wind speed turbulence time series at the 36 <sup>th</sup> story of the building ( $\Delta_t = 0.01$ s) for: (a) $V_{m,10} = 18$ m/s; and (b) $V_{m,10} = 28$ m/s. . . . .	44
5	(a) Force-SDR loop for damping devices at the 23 <sup>th</sup> floor under a frequent wind hazard event with $V_{m,10} = 18$ m/s; and (b) building response in terms of maximum acceleration under the same wind event. . . . .	45
6	Typical sensor measurements at the 5 <sup>th</sup> floor under a given wind load (a) SNR = 1 (no noise); (b) SNR = 0.70 (moderate noise); and (c) SNR = 0.45 (severe noise). . .	46
7	(a) Peak acceleration-related fragility curves representing the effects of motion sickness on the building occupants used for the cost assessment (cost are expressed in USMD), with an identical standard deviation of 0.12 for all curves and individual means $\mu$ reported in the plot; and (b) wind speed hazard curve for the 39-story building using a Weibull distribution with scale parameter 14.9 and shape parameter 6.4. . . . .	47
8	RMSE and NMAE as a function of the training data set size $n$ for uncertainty Cases 1, 2, and 3. . . . .	48
9	Difference of variance (%) for: (a) Case 1; and (b) Case 2 (showing 15 most influential sensors out of 39). . . . .	49
10	Probability density function under uncertainty Case 1: (a) cost of failure; (b) life-cycle cost. . . . .	50
11	Probability density function under uncertainty Case 2: (a) cost of failure; (b) life-cycle cost. . . . .	51

12 Maximum acceleration response profile for no redundancies and under wind speeds:  
(a)  $V_{m,10} = 23$  m/s; and (b)  $V_{m,10} = 28$  m/s. . . . . 52

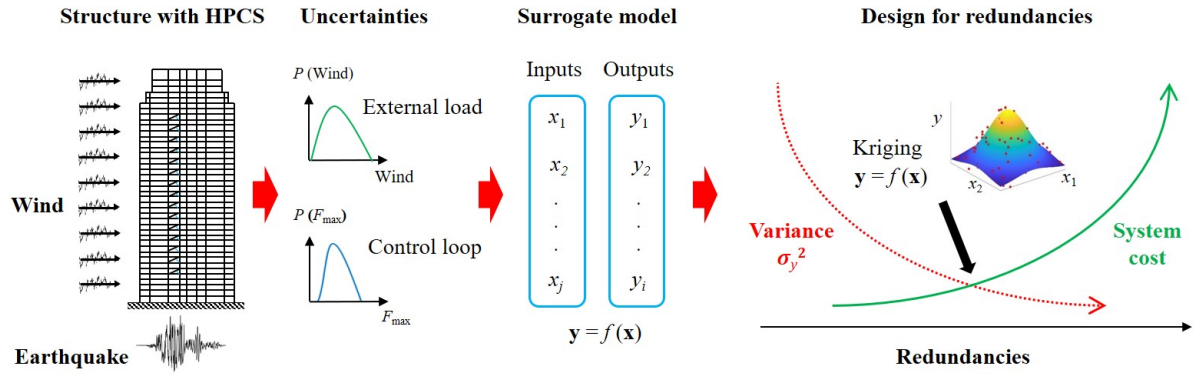


FIG. 1: Schematic illustration of robust design methodology for HPCS systems under uncertainties.

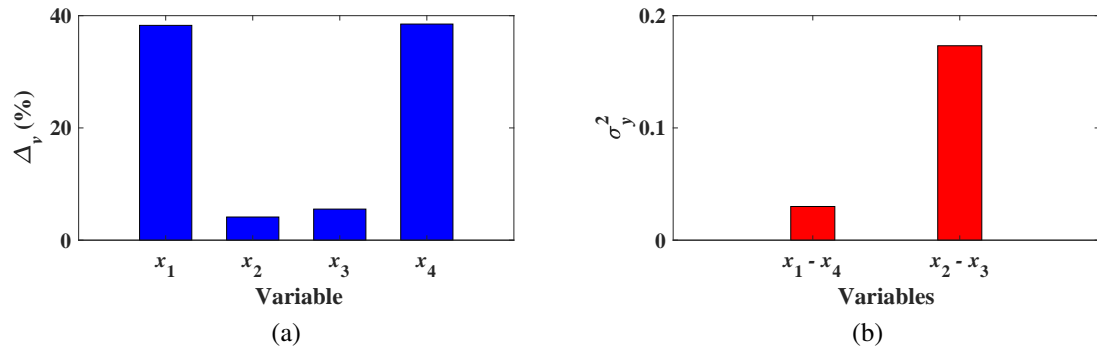


FIG. 2: Analysis of function from Eq. 1: (a) identification of most influential variables; and (b) variance of the system fixing different variables.

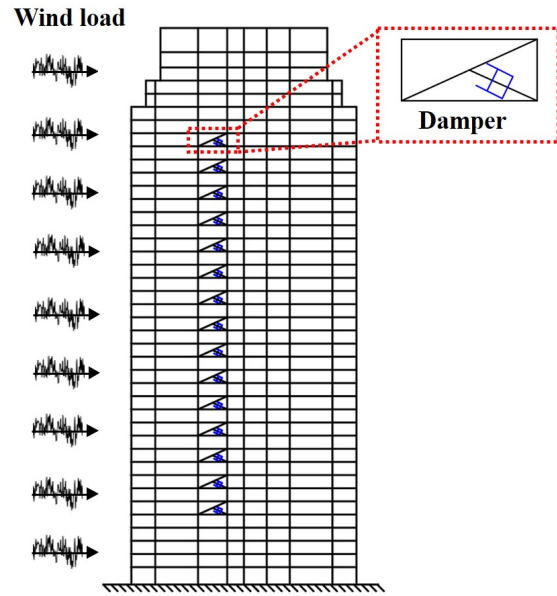
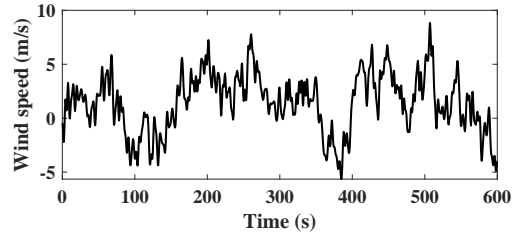
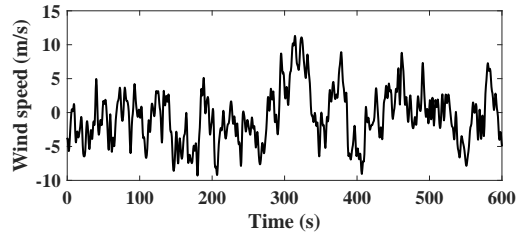


FIG. 3: Schematic representation of the case study building.



(a)



(b)

FIG. 4: Examples of wind speed turbulence time series at the 36<sup>th</sup> story of the building ( $\Delta_t = 0.01$  s) for: (a)  $V_{m,10} = 18$  m/s; and (b)  $V_{m,10} = 28$  m/s.

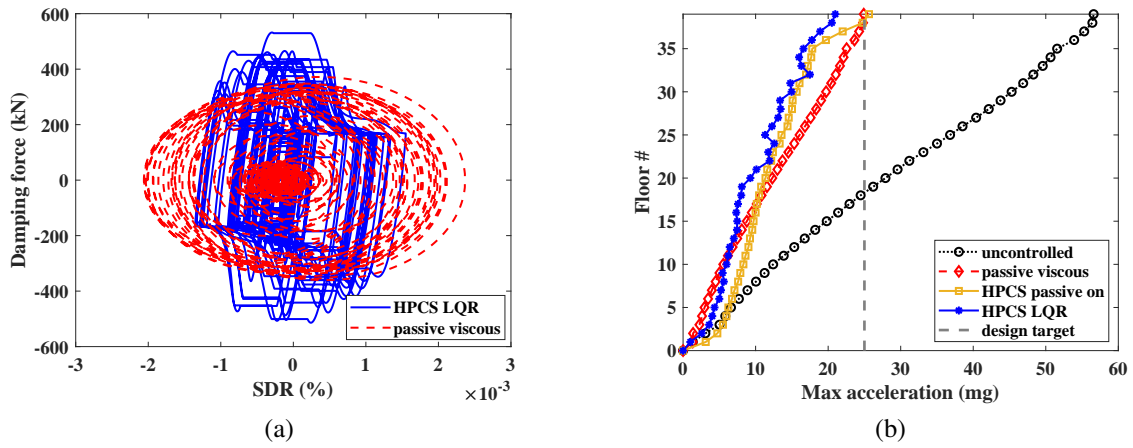
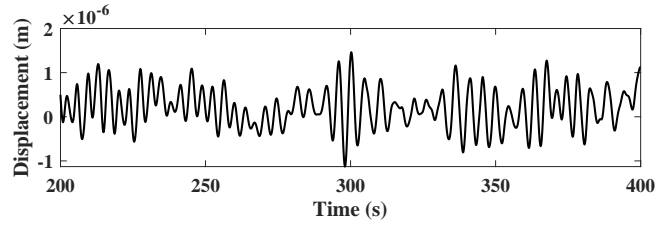
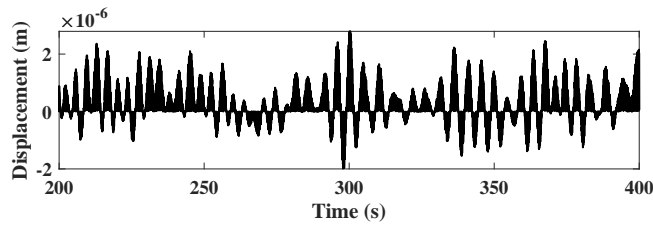


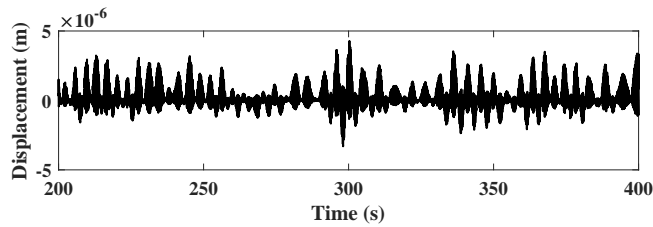
FIG. 5: (a) Force-SDR loop for damping devices at the 23<sup>th</sup> floor under a frequent wind hazard event with  $V_{m,10} = 18$  m/s; and (b) building response in terms of maximum acceleration under the same wind event.



(a)



(b)



(c)

FIG. 6: Typical sensor measurements at the 5<sup>th</sup> floor under a given wind load (a) SNR = 1 (no noise); (b) SNR = 0.70 (moderate noise); and (c) SNR = 0.45 (severe noise).

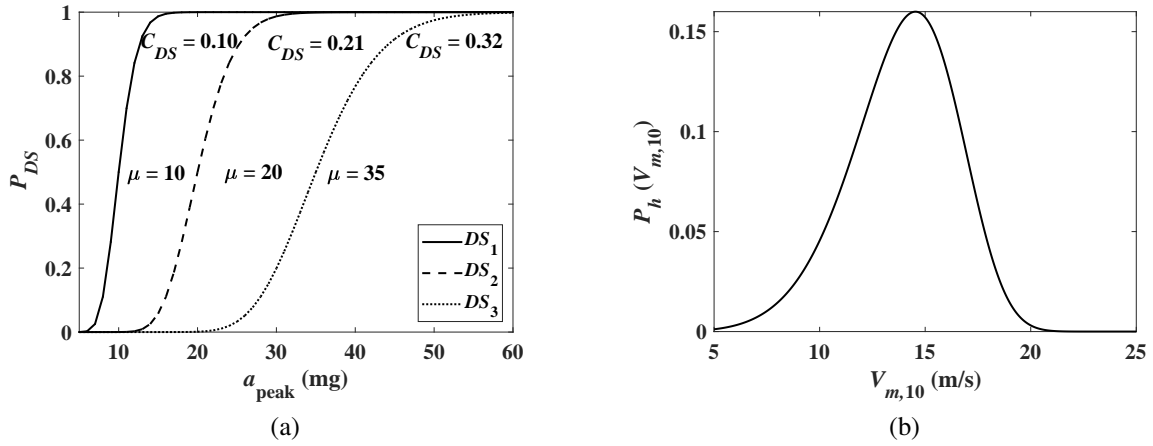


FIG. 7: (a) Peak acceleration-related fragility curves representing the effects of motion sickness on the building occupants used for the cost assessment (cost are expressed in USMD), with an identical standard deviation of 0.12 for all curves and individual means  $\mu$  reported in the plot; and (b) wind speed hazard curve for the 39-story building using a Weibull distribution with scale parameter 14.9 and shape parameter 6.4.

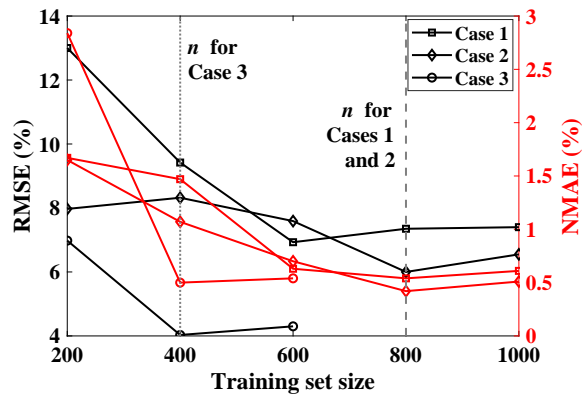
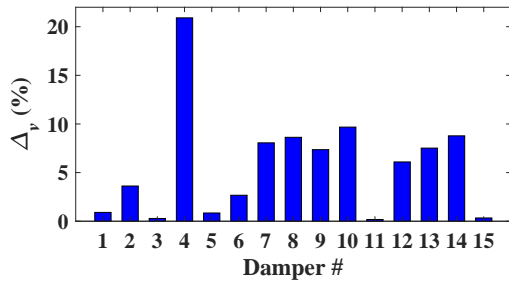
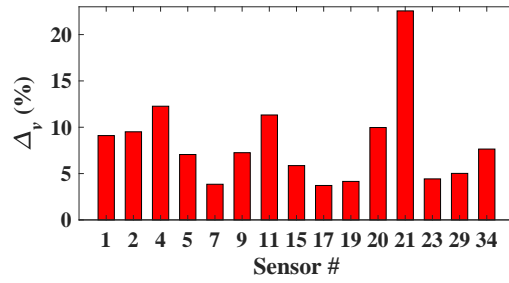


FIG. 8: RMSE and NMAE as a function of the training data set size  $n$  for uncertainty Cases 1, 2, and 3.



(a)



(b)

FIG. 9: Difference of variance (%) for: (a) Case 1; and (b) Case 2 (showing 15 most influential sensors out of 39).

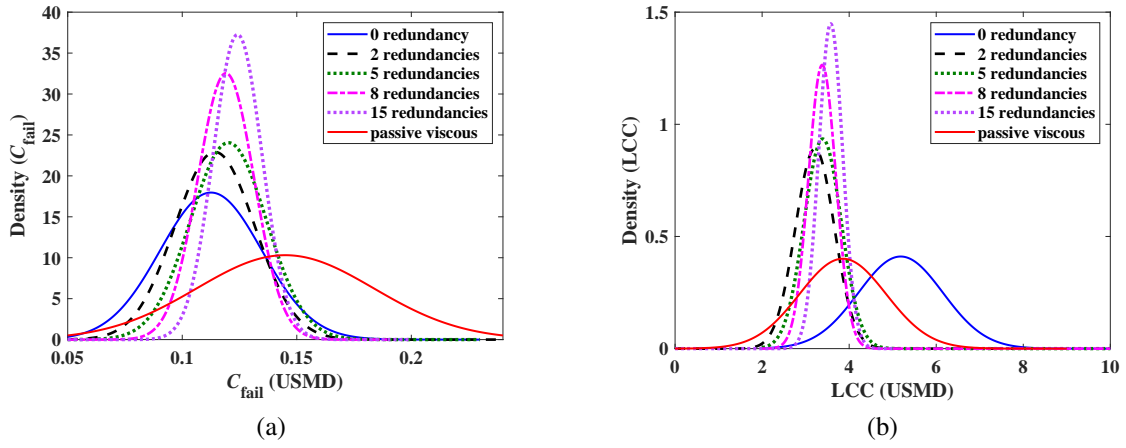


FIG. 10: Probability density function under uncertainty Case 1: (a) cost of failure; (b) life-cycle cost.

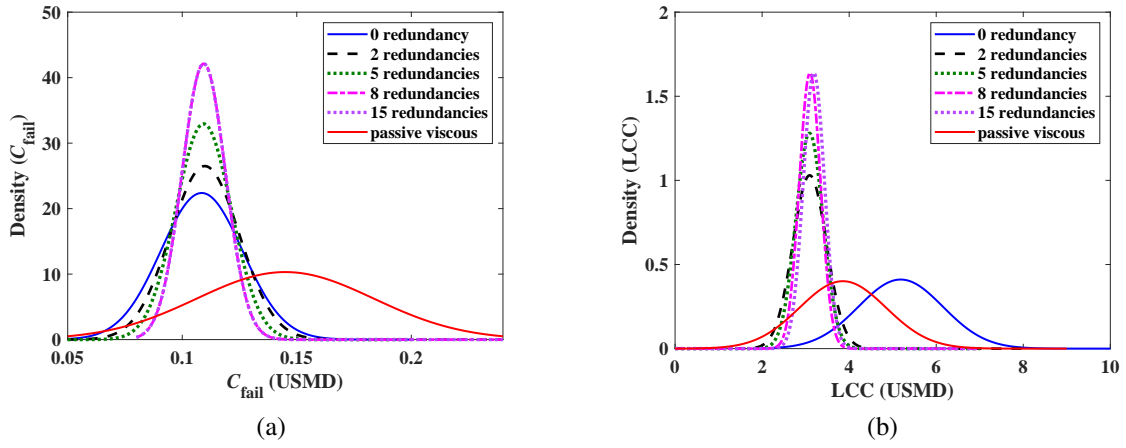
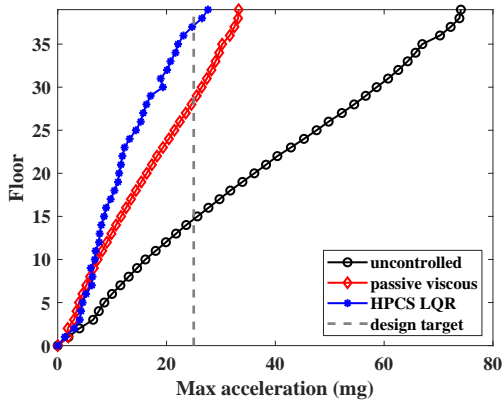
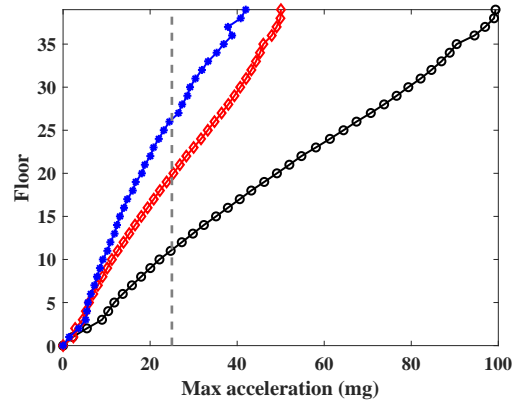


FIG. 11: Probability density function under uncertainty Case 2: (a) cost of failure; (b) life-cycle cost.



(a)



(b)

FIG. 12: Maximum acceleration response profile for no redundancies and under wind speeds: (a)  $V_{m,10} = 23$  m/s; and (b)  $V_{m,10} = 28$  m/s.